

# High-precision co-registration of orbiter imagery and digital elevation model constrained by both geometric and photometric information

Xin Xin<sup>a,b</sup>, Bin Liu<sup>a,\*</sup>, Kaichang Di<sup>a,c</sup>, Mengna Jia<sup>a,b</sup>, Jürgen Oberst<sup>d,e</sup>

<sup>a</sup> State Key Laboratory of Remote Sensing Science, Institute of Remote Sensing and Digital Earth, Chinese Academy of Sciences, No. 20A, Datun Road, Chaoyang District, Beijing 100101, China

<sup>b</sup> University of Chinese Academy of Sciences, Beijing 100049, China

<sup>c</sup> Lunar and Planetary Science Laboratory, Macau University of Science and Technology—Partner Laboratory of Key Laboratory of Lunar and Deep Space Exploration, Chinese Academy of Sciences, Macau, China

<sup>d</sup> Technical University Berlin, Straße des 17. Juni 135, 10623 Berlin, Germany

<sup>e</sup> DLR Institute of Planetary Research, Rutherfordstr. 2, 12489 Berlin, Germany

## ARTICLE INFO

### Keywords:

Co-registration  
Geometric model  
Photometric model  
LRO NAC image  
SLDEM2015  
Lunar mapping

## ABSTRACT

The alignment of images to a reference digital elevation model (DEM) has many applications, especially in planetary exploration. In this paper, we propose a novel high-precision co-registration method for pixel-based matching between an image and a reference DEM to rectify the ever-increasing number of orbiter images to DEMs in a unified reference frame automatically. First, the DEM is converted to a simulated image using a hillshading technique based on a photometric model and the illumination conditions of the image. Then, an initial matching between the simulated and input images is performed based on affine scale-invariant feature transform (ASIFT). The rational function model (RFM) of the image is established and used as a geometric constraint. Then, with tie points (TPs) generated by the initial ASIFT matching, the RFM geometric model of the image is refined, and the gross errors in the TP set are iteratively eliminated. Finally, a high-precision co-registration by pixel-based Least-Squares (LS) image matching is performed using the refined geometric model. Lunar Reconnaissance Orbiter (LRO) Narrow Angle Camera (NAC) and SLDEM2015 (a combined product of Lunar Reconnaissance Orbiter Laser Altimeter (LOLA) and a DEM generated by the Japanese Selenological and Engineering Explorer (SELENE) terrain camera) images are used in our experiment. Results using 17 NAC images at different latitudes demonstrate that the proposed co-registration method is effective and can attain an accuracy of 18.3 pixels in the image space and 25.17 m (0.5 pixel of the reference DEM) in the object space. The method offers an automatic and high-precision matching of LRO NAC images to SLDEM2015. It is also applicable to the co-registration of other orbital images to a reference DEM.

## 1. Introduction

With previous and ongoing planetary exploration missions, significant amounts of orbital data (e.g., images and laser altimetry data) have been acquired. Owing to the precision limitation of orbit and attitude measurements, there are widespread spatial inconsistencies among the multiple-source data such as multi-images and laser-altimetry-derived digital elevation models (DEMs). To fully exploit these data for scientific and engineering applications, it is necessary to co-register the data to a unified reference frame. Co-registration of images to a reference DEM can provide accurate control points for high-precision geometric processing of the images, including geometric model refinement, instrument calibration, and automatic rectification. Another application of the aligned images and DEMs is in the area of

reflectance-based surface reconstruction. The high-precision co-registration of images and DEMs is required when constructing a higher-resolution DEM using a coarse DEM and a high-resolution image using shape-from-shading techniques (Grumpe and Wöhler, 2011, 2014; Wu et al., 2017).

As images and DEMs represent different types of surface information, a pixel-based (area-based) image matching method cannot be applied to an image and DEM registration directly. The co-registration between an image and a DEM is mainly feature-based, such as using craters and ridges (Michael, 2003; Wu et al., 2013). The performance of the feature-based matching method depends on the precision of the feature extraction, which is poor in featureless areas. The precision of feature-based matching methods is typically less than that of pixel-based methods. An approach for the registration of stereo images and a

\* Corresponding author.

E-mail address: [liubin@radi.ac.cn](mailto:liubin@radi.ac.cn) (B. Liu).

<https://doi.org/10.1016/j.isprsjprs.2018.06.016>

Received 4 April 2018; Received in revised form 22 June 2018; Accepted 23 June 2018

Available online 03 July 2018

0924-2716/ © 2018 International Society for Photogrammetry and Remote Sensing, Inc. (ISPRS). Published by Elsevier B.V. All rights reserved.

DEM (or laser altimeter points) is based on a combined block adjustment where 3-dimensional (3D) laser altimeter points are back-projected to the stereo images and used as conjugate points (Soderblom and Kirk, 2003; Yoon and Shan, 2005; Wu et al., 2014). The altitude of the DEM or laser altimetry measurements is used as a constraint equation in block adjustment processing. Another approach for the registration of lunar stereo images and a DEM (or laser altimeter points) is based on surface matching using the iterative closest point algorithm (Di et al., 2012). However, these two approaches for the co-registration of stereo images and a DEM are not applicable to the co-registration of a single image and a reference DEM.

It should be noted that the matching methods mentioned above do not consider the radiometric information during the image in the matching process. In a previous research, pixel-based methods for matching imagery with DEMs considering radiometric information were proposed using earth observation data (Horn and Bachman, 1978). To perform the traditional pixel-based matching method, the simulated image with radiometric information was generated from a DEM by illuminating it with the illumination geometry information of the real image. This method was designed based on the assumption that the DEM itself, as well as its gradients, could be considered as an illumination-invariant representation of the image (Horn, 1977). This assumption does not hold in areas with a variety of surface features, especially in human settlements. Thus, this method was studied only in mountainous terrain without vegetative coverage.

Conversely, on the barren surfaces of the moon and Mars, this method would be more applicable. Similar studies of co-registration between altimeter tracks and images (Soderblom et al., 2002; Soderblom and Kirk, 2003; Nefian and Coltin, 2014) were also based on this assumption. These methods considered the radiometric information of the images; however, because of the large sampling interval of the laser altimeter, the quality of the simulated images was poor, limiting the precision of the co-registration. Thus, these methods are not widely used.

Based on the above literature review of matching methods for orbiter images and reference elevation data, we propose a novel method of pixel-based co-registration of lunar images and DEMs using both geometric and photometric constraints. First, the simulated image is generated based on the illumination condition of the orbital images. The rigorous sensor model (RSM) and rational function model (RFM) of the orbital image are established based on the SPICE (the abbreviation for Spacecraft, Planet, Instrument, Camera-Matrix, and Events) kernels (NAIF, 2014). Then, Harris feature points (Harris and Stephens, 1988) are extracted from the simulated image and back-projected to the orbital image as the initial matching tie points (TPs). Subsequently, a high-precision co-registration based on Least-Squares (LS) image matching is performed using a refined geometric model. From the co-registration, the RFM of the image is refined, and high-precision TPs between the image and the reference DEM are extracted simultaneously. Lunar Reconnaissance Orbiter (LRO) Narrow Angle Camera (NAC) images (Robinson et al., 2010) and SLDEM2015 (a combined product of Lunar Reconnaissance Orbiter Laser Altimeter (LOLA) and a DEM generated by Japanese Selenological and Engineering Explorer (SELENE) terrain camera images, Barker et al., 2016) images at different latitudes are used for experimental tests and validation of the proposed co-registration method.

## 2. Methodology

In the proposed method, the image is co-registered to a reference DEM through a pixel-based matching method using both geometric and photometric constraints. The framework of the proposed method is outlined in Fig. 1. Because the DEM has significantly lower resolution (60 m/pixel at equator) than the images (approximately 1.5 m/pixel) used in our experiments, we first upsample the DEM to the image resolution based on spline interpolation (Franke, 1982; Mitas and

Mitasova, 1988). Then, the simulated images are generated using a hillshading technique based on the illumination conditions of the images. To obtain initial matching TPs and starting solution for the LS image matching, affine scale-invariant feature transform (ASIFT, Morel and Yu, 2009) is performed between the simulated and actual orbital images.

The RSM of the orbital image is established (Liu et al., 2017) based on the SPICE kernels. The RFM of the image is established based on the RSM and is used as a geometric constraint in the co-registration process. With TPs generated by the initial ASIFT matching, the RFM of the image is refined, and the gross errors of the TPs are iteratively eliminated. Then, evenly distributed feature points are generated on the simulated image and are projected onto the orbital image as predicted matching positions using the refined RFM. Finally, a high-precision co-registration based on LS image matching is performed and the geometric model is further refined.

### 2.1. Image simulation using DEM

In our research, image simulation is based on the hillshading technique. The key to this method is to present the reflectance of a small, flat surface as a function of the gradient of the terrain. An idealized reflectance model (the surface is assumed to be an ideal diffuser or Lambertian surface) is used in this case to establish the function (Eq. (1)) (Horn and Bachman, 1978; Horn, 1981) on the moon.

$$\Phi(p, q) = \rho \cos(i) / \cos(e) = \frac{\rho(1 + p_s p + q_s q)}{\sqrt{1 + p_s^2 + q_s^2}}$$

$$p_s = \sin(\theta) \cot(\phi), \quad q_s = \cos(\theta) \cot(\phi) \quad (1)$$

where  $\Phi(p, q)$  is the calculated simulated pixel intensity,  $i$  is the incidence angle,  $e$  is the emission angle,  $\rho$  is an albedo factor,  $\theta$  is the solar azimuth of each image,  $\phi$  is the solar altitude of each image (Fig. 2),  $p$  and  $q$  are the gradients of the surface in the line and sample direction, respectively, which can be estimated using the first-order differences of a small, flat surface of the DEM (Horn, 1981).

In this research,  $p$  and  $q$  for each pixel in the DEM are estimated based on eight-neighbor grid elevations. The solar azimuth and solar altitude used in Eq. (1) can be retrieved from the header file of the image. Then, the pixel intensity in the simulation image is calculated with the reflectance model. In the result, the simulated image has an illumination condition similar to that of the real image. The simulated image becomes a “bridge” to connect the DEM and the orbital image in pixel-based matching.

### 2.2. RFM and its refinement model

The RFM, which establishes the relationship between the image-space coordinates and object-space coordinates with the ratios of polynomials, is displayed in Eq. (2) (Di et al., 2003).

$$r = \frac{P_1(X, Y, Z)}{P_2(X, Y, Z)}$$

$$c = \frac{P_3(X, Y, Z)}{P_4(X, Y, Z)} \quad (2)$$

The three-order polynomials  $P_i$  ( $i = 1, 2, 3$ , and 4) have the following general form:

$$P_i(X, Y, Z) = a_1 + a_2 X + a_3 Y + a_4 Z + a_5 XY + a_6 XZ + a_7 YZ + a_8 X^2$$

$$+ a_9 Y^2 + a_{10} Z^2 + a_{11} XYZ + a_{12} X^3 + a_{13} XY^2 + a_{14} XZ^2$$

$$+ a_{15} X^2 Y + a_{16} Y^3 + a_{17} YZ^2 + a_{18} X^2 Z + a_{19} Y^2 Z + a_{20} Z^3 \quad (3)$$

where  $a_1, a_2 \dots a_{20}$  are the coefficients of the polynomial function  $P_i$ , called the rational polynomial coefficients (RPCs). Construction of an RFM is a process of fitting the vast number of virtual points generated based on the RSM through an LS solution (Liu and Di, 2011; Liu et al., 2016). The RFM is considerably simpler and more independent of

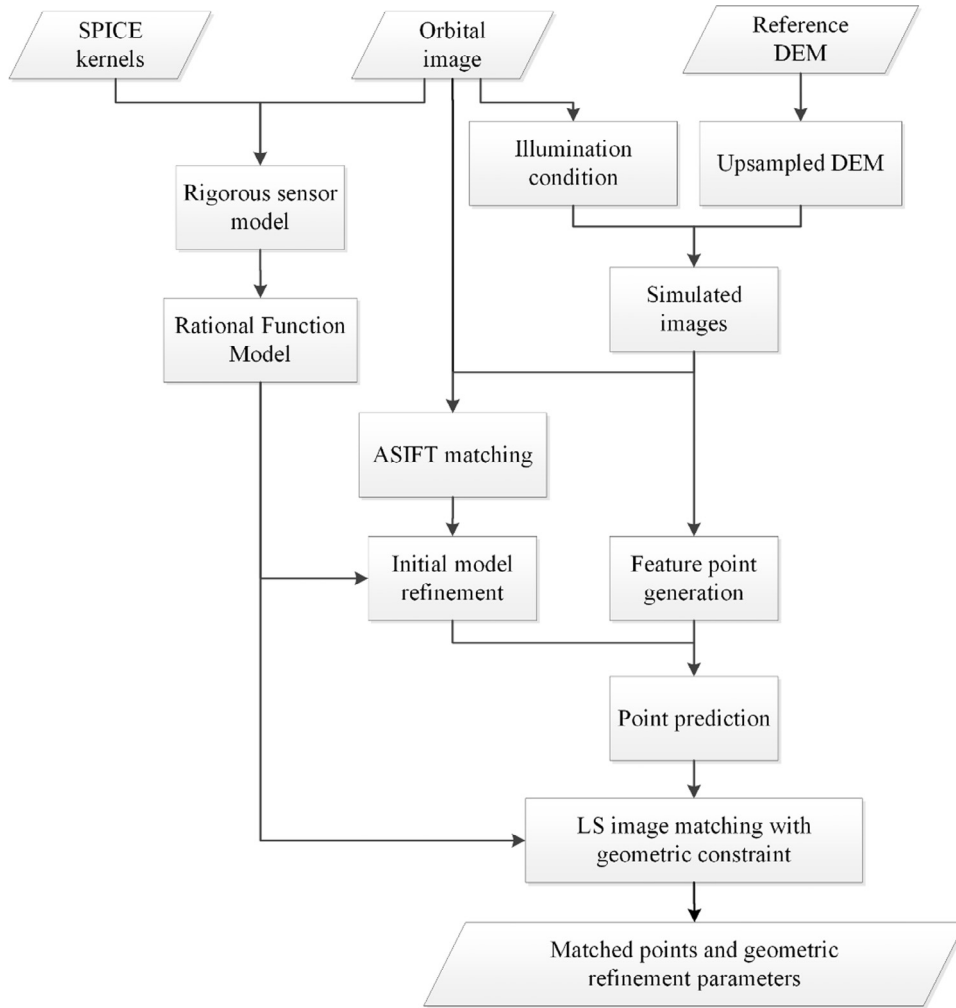


Fig. 1. Flowchart of the proposed method.

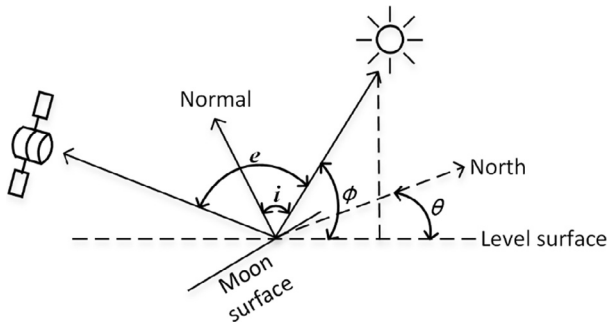


Fig. 2. Schematic of the factors that influence the intensity of reflectance from the lunar surface.

sensors than the RSM, and the RFM can fit the RSM without a loss of accuracy.

Typically, the RFM of a lunar orbital image contains biases caused by the precision limitations of the orbit and attitude measurements. The biases are reflected by back-projection errors in the image space, and can be corrected through the co-registration of the image and a reference DEM. The affine transformation model (Liu et al., 2014) in image space, displayed in Eq. (4), is used to correct the biases to refine the RFM.

$$\begin{aligned} F_r &= a_0 + a_1c' + a_2r' - r = 0 \\ F_c &= b_0 + b_1c' + b_2r' - c = 0 \end{aligned} \quad (4)$$

where  $(r, c)$  are the measured (matched) image coordinates,  $(r', c')$  are the back-projected image coordinates of the TPs calculated from the ground points using an RFM, and  $a_0, a_1, a_2, b_0, b_1,$  and  $b_2$  are affine transformation parameters, i.e., the geometric refinement parameters.

### 2.3. LS image matching with global geometric constraint

The matching method presented in this paper is based on the classic LS image matching method (Ackermann, 1984), which considers both the geometric distortion and radiometric distortion, as displayed in Eq. (5);

$$\begin{aligned} g_1(x, y) + n_1(x, y) &= h_0 + h_1g_2(a_0 + a_1x + a_2y, b_0 + b_1x + b_2y) \\ &+ n_2(x, y) \end{aligned} \quad (5)$$

where  $g_1$  and  $g_2$  are the functions of the intensity value in the conjugate regions of the stereo images,  $n_1$  and  $n_2$  are the noise,  $x, y$  are the coordinates of a TP in the reference image,  $a_0, a_1, a_2, b_0, b_1,$  and  $b_2$  are the geometric affine transformation parameters, and  $h_0, h_1$  are parameters of the radiometric transformation between the conjugate regions. However, the classic LS matching method only considers the geometric distortion in a single conjugate region and does not consider the geometric transformations among all matched TPs. This can lead to a less robust matching result between the image and DEM.

In this paper, we present an LS matching method with global geometric constraints to improve the matching robustness. With the geometric information obtained in Section 2.2, the geometric distortions

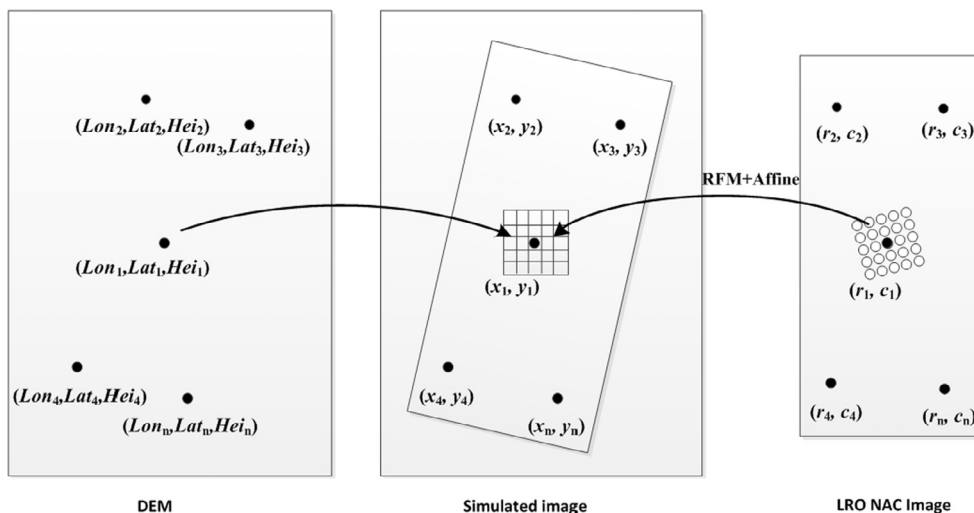


Fig. 3. Schematic of LS matching with global geometric constraint.

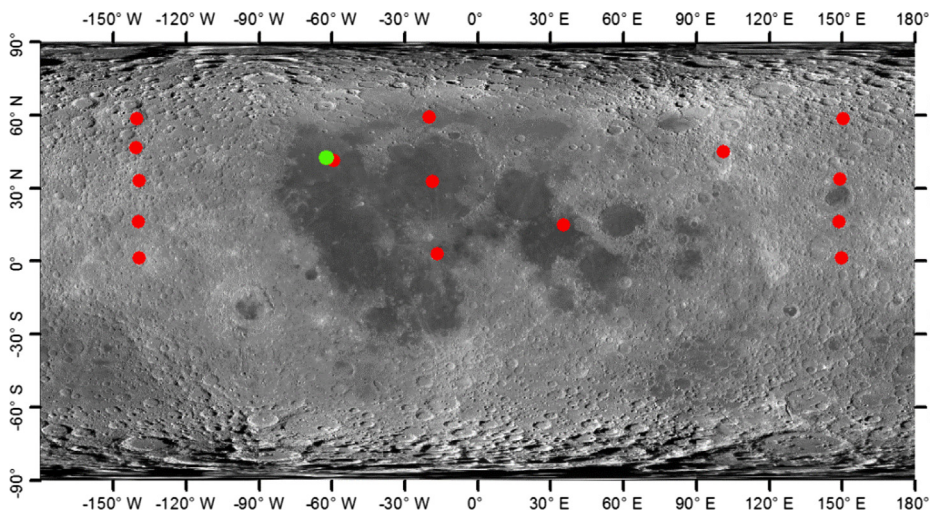


Fig. 4. Locations of images used in the experiment. Green point represents two overlapping locations of the images selected from Chang'E-5 preselected landing site. Red points represent locations of images distributed at different latitudes. (For interpretation of the references to color in this figure legend, the reader is referred to the web version of this article.)

among all TPs are considered using the RFM and refinement model in the matching process. Eq. (6) displays the function of the improved LS matching.

$$g_1(x, y) + n_1(x, y) = h_0 + h_1 g_2(r, c) + n_2(x, y) \quad (6)$$

$$\begin{aligned} r &= a_0 + a_1 c' + a_2 r' + \delta_r \\ c &= b_0 + b_1 c' + b_2 r' + \delta_c \end{aligned} \quad (7)$$

where  $x, y$  are the coordinates of a TP in the simulated image (equivalently in the reference DEM),  $r$  and  $c$  are the coordinates that are calculated through RPCs and the refined transformation parameters,  $\delta_r$  and  $\delta_c$  are the geometric model errors, and  $r'$  and  $c'$  are the coordinates calculated from Eq. (2). Using Eq. (6), every pixel in the image patch centered at each TP provides an error equation. Eq. (7) is used as an additional equation in the adjustment to impose a global geometric constraint. A virtual observation equation is presented to constrain the geometric transformation parameters (Eq. (8));

$$\delta_r = 0, \quad \delta_c = 0 \quad (8)$$

Before the global LS image matching, the initial values of the unknowns (i.e., the affine transformation parameters and the coordinates of TPs) must be first calculated. The initial values of the geometric transformation parameters are calculated based on the ASIFT matched TPs. Rather than using ASIFT feature points, the Harris feature points are extracted from the simulated image for the LS matching.

Fig. 3 is a schematic illustration of the proposed matching method. The geographic coordinates of the feature points are calculated through the reference DEM. The feature points are back-projected onto the real image based on the initial refined RFM and are used as the initial TPs. The final TPs and refined RFM are adjusted through an iterative procedure in the LS image matching with global geometric constraints.

### 3. Experimental analysis

#### 3.1. Datasets

In our experiment, 17 LRO NAC images and SLDEM2015 were used to test and validate the developed method. Two of the LRO NAC images were located at the preselected landing site of the Chang'E-5 mission, China's first sample return mission, which is scheduled to land near Mons Rümker in Oceanus Procellarum in 2019 (Gbtimes, 2017; Xinhuanet, 2017); the other 15 images were distributed at different latitudes. All experimental data were downloaded from the Planetary Data Systems (PDS) website (<http://ode.rsl.wustl.edu/moon/>). In this research, the resolution of the NAC images chosen for this experiment was approximately 1.5 m/pixel. SLDEM2015 was chosen as the reference DTM. It is a combined product of LOLA and a DEM generated by SELENE terrain camera images covering latitudes within  $\pm 60^\circ$ , at a horizontal resolution of 512 pixels per degree (an effective resolution of approximately 60 m at the equator) and a vertical accuracy from

**Table 1**  
Main parameters of images used in the experiment.

| Image ID      | Center latitude (°) | Center longitude (°) | Resolution (m) | Incidence angle (°) | Sub solar azimuth (°) |
|---------------|---------------------|----------------------|----------------|---------------------|-----------------------|
| M1173478556LE | 42.35               | -62.3                | 1.43           | 73.89               | 197.68                |
| M1188747453LE | 42.35               | -62.16               | 1.26           | 71.17               | 196.68                |
| M1143826200LE | 1.12                | 149.81               | 1.23           | 57.12               | 181.04                |
| M1173968149LE | 1.14                | -139.29              | 1.13           | 61.39               | 181.88                |
| M1096601220LE | 2.86                | -16.49               | 1.12           | 67.72               | 181.54                |
| M1123363232LE | 14.72               | 35.47                | 1.17           | 66.6                | 175.17                |
| M1113197889LE | 15.95               | 148.88               | 1.32           | 55.42               | 191.39                |
| M1097401250RE | 16.03               | -139.41              | 1.39           | 59.84               | 189.38                |
| M1157862745LE | 32.58               | -18.51               | 1.34           | 72.98               | 191.06                |
| M1097393759LE | 32.85               | -139.08              | 1.59           | 63.79               | 198.95                |
| M1205049446RE | 33.56               | 149.26               | 1.40           | 61.05               | 202.13                |
| M1112211163RE | 41.08               | -59.00               | 1.44           | 72.26               | 196.83                |
| M1098172290LE | 44.90               | 101.14               | 1.59           | 62.66               | 211.40                |
| M1189253414LE | 46.34               | -140.54              | 1.49           | 68.45               | 203.51                |
| M1158638171RE | 58.34               | -139.98              | 1.65           | 74.77               | 204.43                |
| M1205056993RE | 58.36               | 150.71               | 1.58           | 72.62               | 211.68                |
| M1111955876LE | 58.86               | -19.76               | 1.54           | 79.09               | 199.17                |

approximately 3 m to 4 m (Barker et al., 2016).

The locations of all images used in the research are displayed in Fig. 4, with the background of an LRO WAC global image mosaic downloaded from the U.S. Geological Survey (USGS) website ([https://astrogeology.usgs.gov/search/details/Moon/LRO/LROC\\_WAC/Lunar\\_LRO\\_LROC-WAC\\_Mosaic\\_global\\_100m\\_June2013/cub](https://astrogeology.usgs.gov/search/details/Moon/LRO/LROC_WAC/Lunar_LRO_LROC-WAC_Mosaic_global_100m_June2013/cub)). The image IDs and their main parameters are listed in Table 1. The solar azimuth and solar altitude of the NAC images are obtained from the headers of the PDS files.

### 3.2. Simulated images and initial value of co-registration

Based on the illumination information of the images, 17 simulated images were generated. Fig. 5 displays a portion of SLDEM2015 and two examples of the simulated images located at the Chang'E-5 pre-selected landing site based on the method described in Section 2.1. As the DEM (Fig. 5(a)) and the real NAC images (Fig. 5(c), (e)) represent

different types of surface information, it is difficult to match the NAC images to the DEM directly based on the LS matching method. The simulated images (Fig. 5(b), (d)) have similar appearances to the real NAC images (Fig. 5(c), (e)), providing the possibility of area-based registration between the images and DEM.

In the simulated images, feature points are detected based on the Harris detector, which computes a matrix related to the autocorrelation function of the image. There is a clear inconsistency between the reference DEM and NAC image with original RPCs (Fig. 8(b, d, f, h, i, j)). Thus, ASIFT matching is performed between the simulated image and the real orbital image to calculate an initial refining parameters of the RPCs. For the detected Harris points in the simulated image, the initial values of their conjugate points in the real image are calculated using the refined RPCs. To achieve higher co-registration precision, it was necessary to co-register the image to a DEM using LS matching and further refine the RPC.

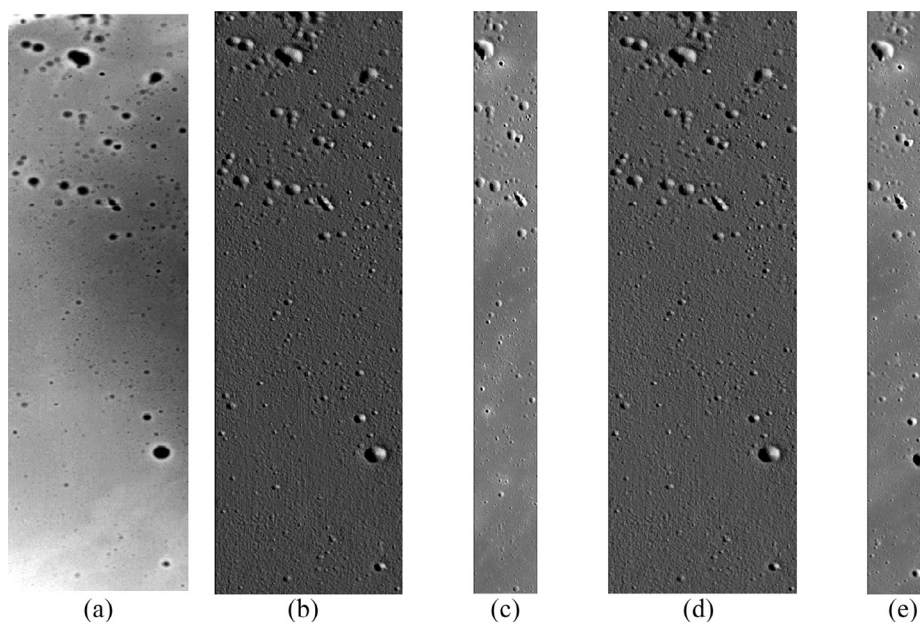


**Fig. 5.** Examples of actual LRO NAC images and simulated images. (a) A portion of SLDEM2015. (b) Simulated image with the same illumination condition as (c). (c) NAC image (image ID: m1173478556le). (d) Simulated image with the same illumination condition as (e). (e) NAC image (image ID: m1188747453le).

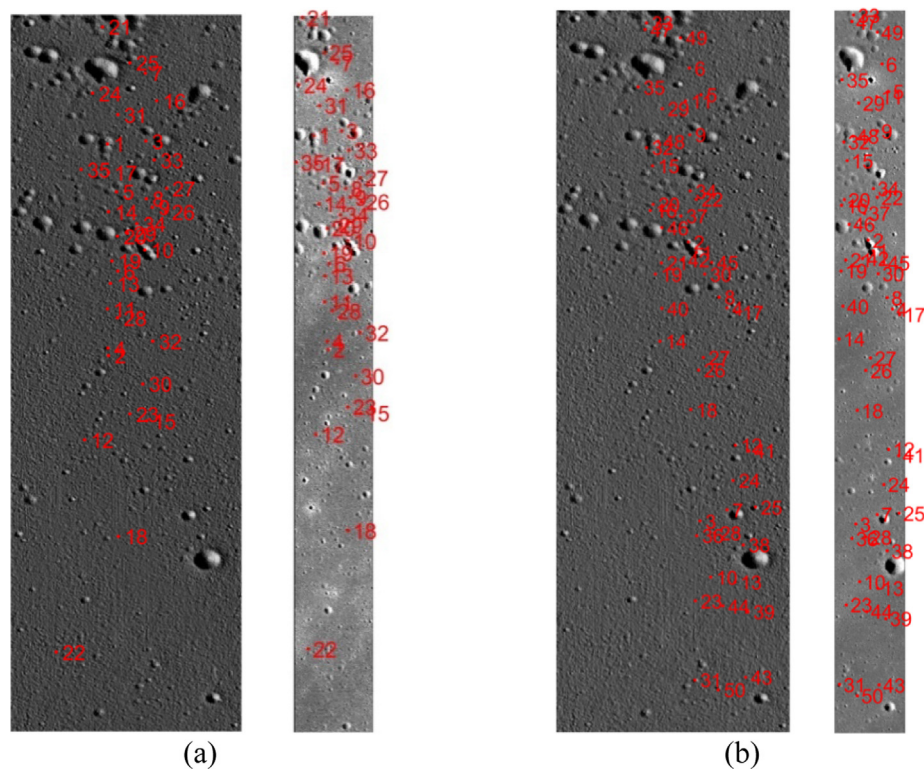


Fig. 6. Distribution of final matched TPs. (a) Image ID: m1173478556le. (b) Image ID: m1188747453le.

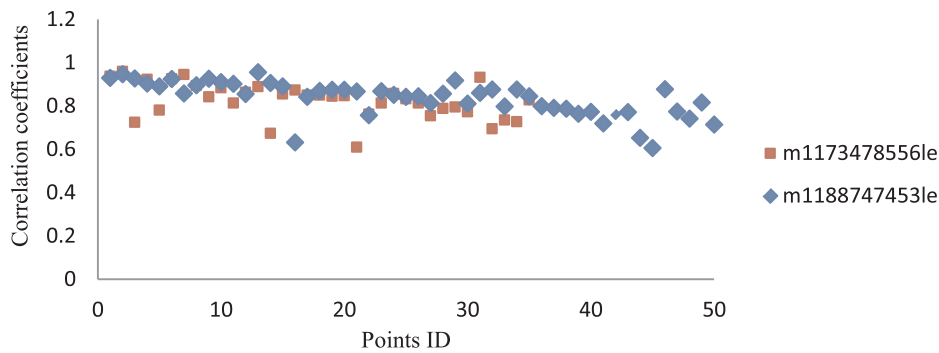


Fig. 7. Correlation coefficients of TPs.

### 3.3. Co-registration results and precision evaluation

Two LRO NAC images at the Chang'E-5 preselected landing site were selected as examples to evaluate the precision of this method in detail. Using the method described in Section 2.3, 216 and 179 feature points were extracted from the two images. The TPs whose correlation coefficients were greater than 0.7 were selected as final TPs. Fig. 6 displays the distribution of the final matched TPs. All TPs were evenly distributed over the overlapping area between the image and the DEM. Thus, the image can be well rectified in all positions of the image. Fig. 7 displays the correlation coefficients of the TPs, indicating a high matching precision.

Based on the initial RPCs and refinement parameters, two NAC orthophotos were generated. The position difference between the orthophotos and reference DEM are indicated in Fig. 8. Three typical craters are chosen as examples from the two NAC images. The color part is the reference DEM; the grayscale part of the figure is the orthophoto. There is a spatial inconsistency between the original orthophotos and the DEM in Fig. 8(b, d, f, h, i, j).

In Fig. 8(c, e, g, k, l, m), the inconsistency is eliminated through the proposed co-registration method. Furthermore, the orthophotos are

draped on the reference DEM to verify their consistency with the DEM. Fig. 9 displays the local area of the draping result. In the orthophoto generated from the original RPC, it is easy to determine that the shadow area is higher than the rim of the crater, and the bright area is lower than the rim of the crater (Fig. 9(a)). This is clearly unreasonable. Conversely, the orthophoto generated from the refined RPC is considerably more reasonable, indicating a superior consistency with the DEM (Fig. 9(b)).

To further quantitatively evaluate the co-registration precision, the matching results of feature-based matching, ASIFT matching, classic LS matching, and the proposed global LS matching method were compared. In the feature-based matching method, the centers of the craters, which were extracted manually through CraterTools (Kneissl et al., 2011), were chosen as the TP feature. There were 62 (image ID: m1173478556le) and 64 (image ID: m1188747453le) pairs of craters chosen from the two orbital images and SLDDEM2015. Table 2 presents the precision of the co-registration represented by the fitting precision (the RMSE in image space) of the affine transformation for RFM refinement. For the Chang'E-5 preselected landing site, the proposed method attained a mean accuracy of 15.6 pixels in the image space and 20.95 m (approximately 0.5 pixel of the reference DEM) in the object

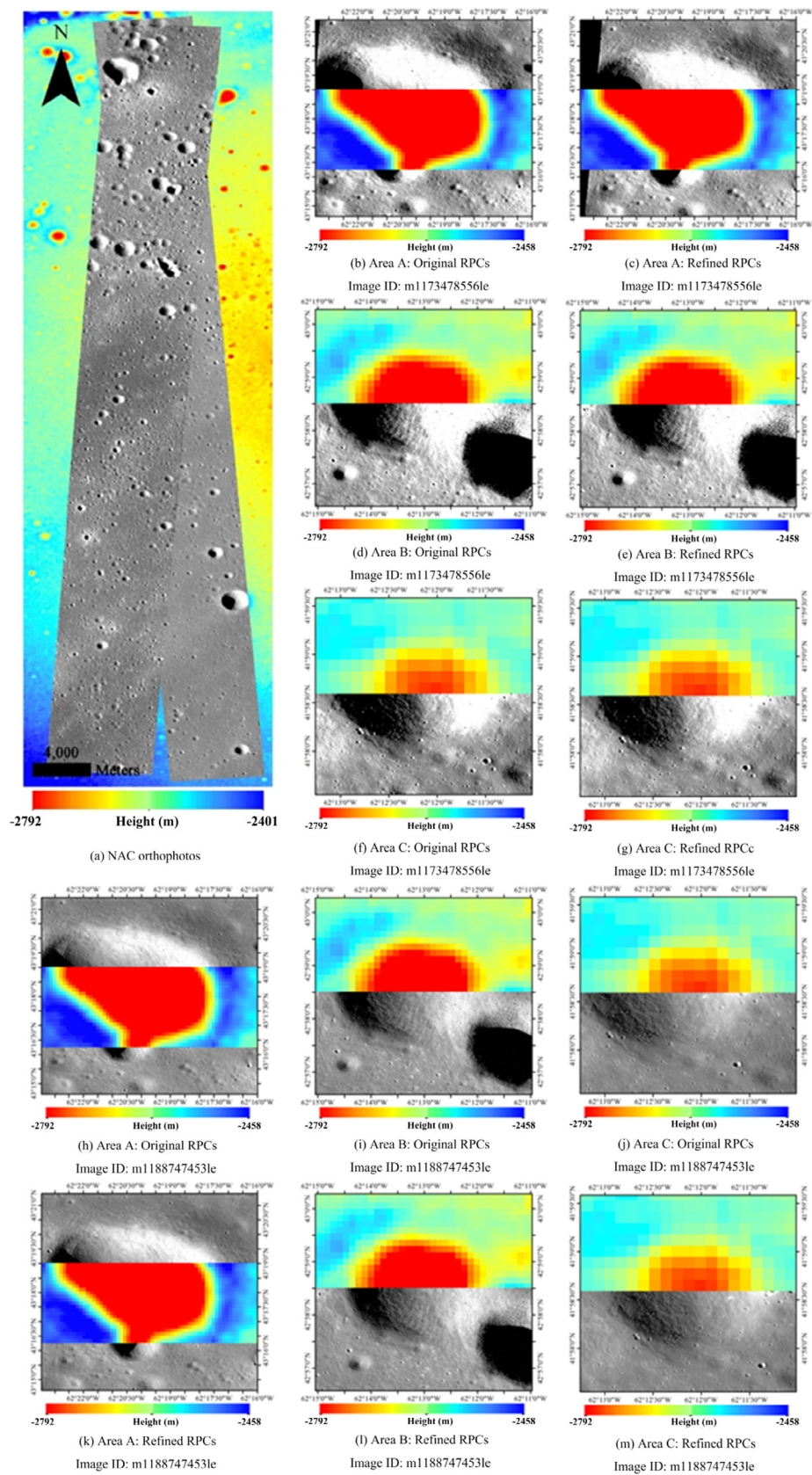


Fig. 8. Position difference between orthophotos and reference DEM.

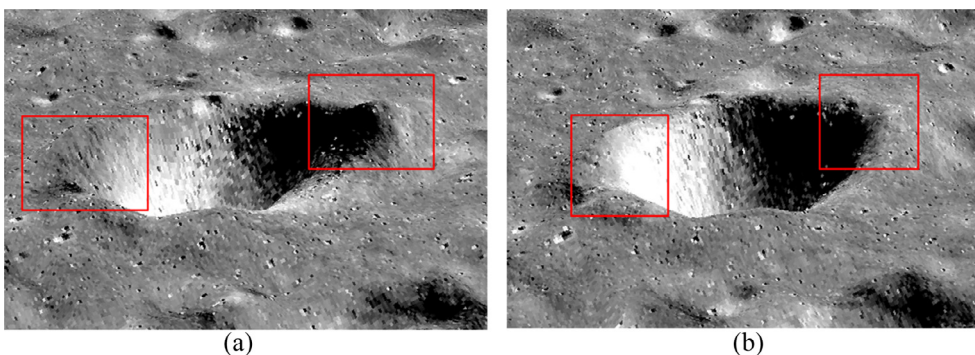


Fig. 9. Local area of orthophotos draped on reference DEM. Image ID: m1173478556le. (a) Orthophoto generated using original RPCs. (b) Orthophoto generated using refined RPCs.

Table 2  
Matching precisions of different methods.

| Method                | Image ID      | RMSE/X (pixel) | RMSE/Y (pixel) | RMSE/All (pixel) |
|-----------------------|---------------|----------------|----------------|------------------|
| Feature-based method  | m1173478556le | 13.930         | 15.133         | 20.568           |
|                       | m1188747453le | 17.651         | 15.048         | 23.194           |
| ASIFT                 | m1173478556le | 9.532          | 20.980         | 23.044           |
|                       | m1188747453le | 19.863         | 24.036         | 31.181           |
| Traditional LS method | m1173478556le | 12.241         | 15.424         | 19.691           |
|                       | m1188747453le | 9.772          | 16.255         | 18.966           |
| Proposed method       | m1173478556le | 8.729          | 12.511         | 15.256           |
|                       | m1188747453le | 8.354          | 13.566         | 15.932           |

space. This indicates that the precision of the proposed method was greater than that of the other three methods (Table 2). Further, the precision of the proposed method was 1.5 or 2 times greater than the precision of the feature-based and ASIFT methods.

### 3.4. Co-registration results at different latitudes

During the course of the experiment, we realized that different simulated images contained dissimilar amounts of information. The higher the latitude, the finer the DEM. Clearly, the simulated images would have a greater information quantity using a finer DEM (see examples in Fig. 10). Based on this observation, additional image co-

registration experiments were performed at different latitudes. The interval of the latitude was 10°, and three images at different longitudes were chosen at each latitude.

The results of ASIFT matching, classic LS matching, and the proposed matching method at different latitudes were compared by considering the distribution of the TPs and the precision of co-registration. The result at each latitude was averaged over of the three images captured at different longitudes. Fig. 11 displays the number of TPs extracted using the three different matching methods. The proposed method extracted the greatest number of TPs, nearly twice the number of TPs as extracted by ASIFT. The distribution of the TPs extracted from ASIFT was concentrated in several craters or rocks, whereas the distributions of the TPs extracted from the classic LS matching and proposed matching method were evenly distributed. This ensures that LS matching can rectify the image well in every region of the image.

Fig. 12 displays the precision of the proposed method, the traditional pixel-based matching method, and the ASIFT matching method at different latitudes. It can be clearly seen that the matching precision improves with an increase in latitude. This trend is consistent with the quality of the DEM at different latitudes (the higher the latitude, the higher the resolution of the DEM). The proposed method attained a mean accuracy of 18.3 pixels in the image space and 25.17 m (approximately 0.5 pixel of the reference DEM) in the object space. Compared with ASIFT matching, the precision of the proposed method increased 38.3%, in particular at low latitudes. In the majority of regions, the matching result of the proposed method was marginally better than the one of the traditional LS matching method. Considering that the

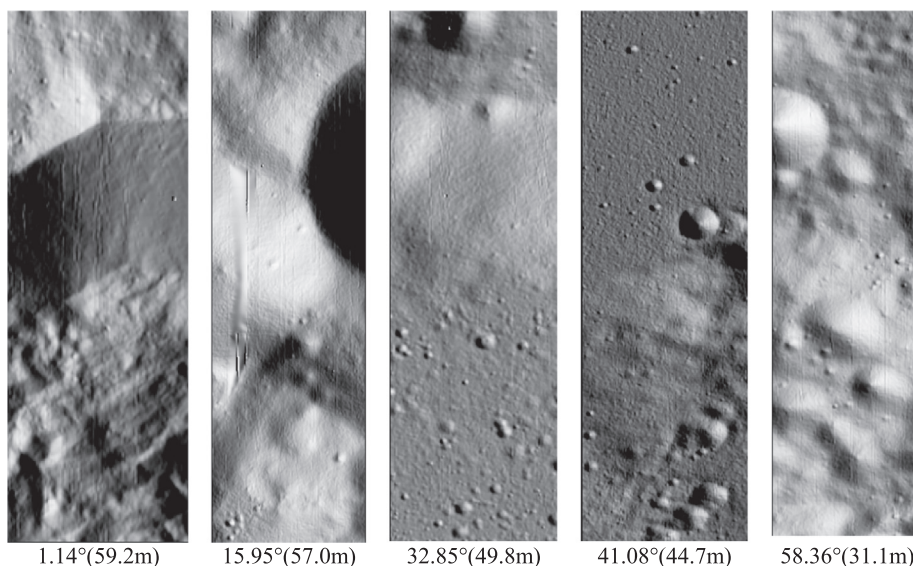


Fig. 10. Examples of simulated images located at different latitudes. The resolution of SLDEM2015 at different latitude is indicated in the parentheses.

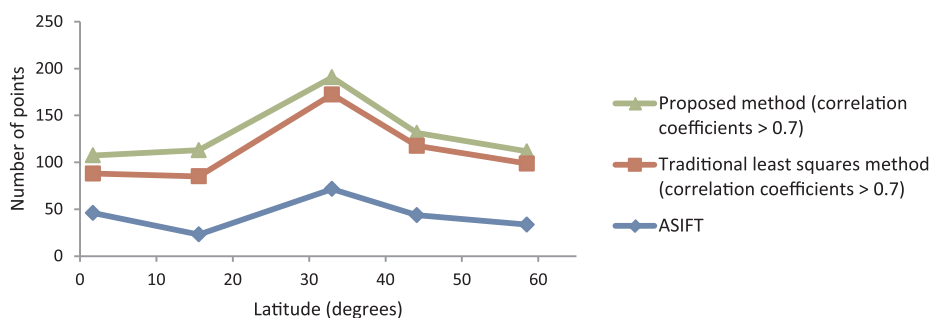


Fig. 11. Number of matched TPs at different latitudes.

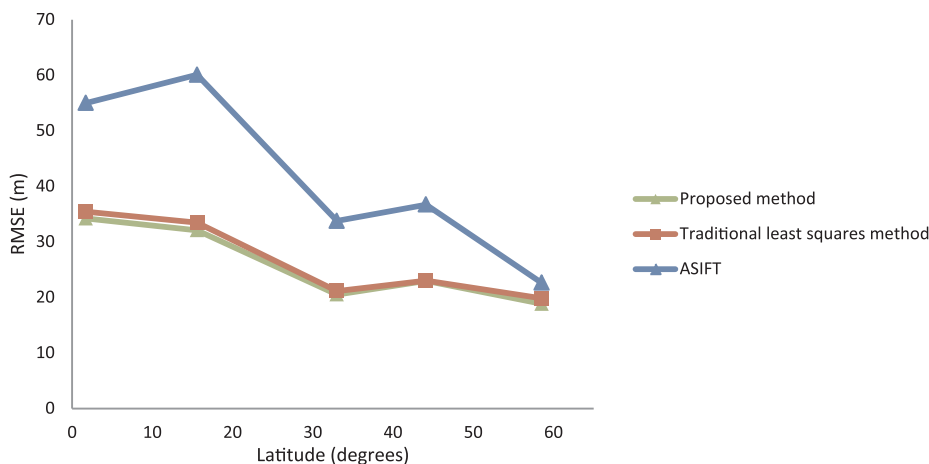


Fig. 12. Precision (RMSE in meters) of co-registration methods at different latitudes.

proposed method can obtain more TPs (as indicated in Fig. 11), it is not only more accurate but also more robust.

#### 4. Conclusions

In this paper, a novel pixel-based method using both geometric and photometric constraints for the co-registration of lunar orbital images and reference DEMs was presented. During the co-registration, the orientation of the image was also refined. This facilitates the subsequent orthophoto generation. Experiments using 17 NAC images and SLDEM2015 demonstrated the feasibility and effectiveness of the proposed method. The precision of the co-registration achieved a subpixel level of the reference DEM. Further, the proposed co-registration method outperformed the ASIFT matching and traditional LS methods. The proposed method offers a high-precision and automatic method of matching orbiter images to DEMs. Moreover, we studied the accuracy of co-registration between LRO NAC images and SLDEM2015 at different latitudes. We determined that the precision improved virtually linearly with latitude increase. Thus, the denser the DEM, the more efficient the proposed method.

Because of the significant resolution differences between the LRO NAC images and the reference DEMs, spatial inconsistencies can exist in the overlapping areas of the adjacent images if they are registered to the reference DEMs separately. Future research will focus on the simultaneous co-registration of multiple adjacent images to a reference DEM to support automated large area seamless orthorectification.

#### Acknowledgments

This study was supported by the Key Research Program of the Chinese Academy of Sciences (Grant No. XDPB11) and National Natural Science Foundation of China (Grant Nos 41771490, 41671458, and 41590851). We thank all those who worked on the Planetary Data

System archive to make the LRO imagery and SLDEM2015 publicly available. We also thank the editor and two anonymous reviewers for their careful proofreading and helpful comments.

#### References

- Ackermann, F., 1984. Digital image correlation: performance and potential application in photogrammetry. *Photogram. Rec.* 11 (64), 429–439.
- Barker, M.K., Mazarico, E., Neumann, G.A., Zuber, M.T., Haruyama, J., Smith, D.E., 2016. A new lunar digital elevation model from the Lunar Orbiter Laser Altimeter and SELENE Terrain Camera. *Icarus* 273, 346–355.
- Di, K., Hu, W., Liu, Y., Peng, M., 2012. Co-registration of Chang'E-1 stereo images and laser altimeter data with crossover adjustment and image sensor model refinement. *Adv. Space Res.* 50, 1615–1628.
- Di, K., Ma, R., Li, R.X., 2003. Rational functions and potential for rigorous sensor model recovery. *Photogramm. Eng. Remote Sens.* 69 (1), 33–41.
- Franke, R., 1982. Smooth interpolation of scattered data by local thin plate splines. *Comput. Math. Appl.* 8 (4), 273–281.
- Gbtimes, 2017. < <https://gbtimes.com/china-confirms-landing-site-change-5-moon-sample-return> > (accessed 19 May 2018).
- Grumpe, A.M., Wöhler, C., 2011. DEM construction and calibration of hyperspectral images data using pairs of radiance images. In: *Proceedings of the IEEE International Symposium on Image and Signal Processing and Analysis*. pp. 609–614.
- Grumpe, A., Wöhler, C., 2014. Recovery of elevation from estimated gradient fields constrained by digital elevation maps of lower lateral resolution. *ISPRS J. Photogramm. Remote Sens.* 94, 37–54.
- Harris, C., Stephens, M., 1988. A combined corner and edge detector. In: *Proceedings of the 4th Alvey Vision Conference*. pp. 147–151.
- Horn, B.K.P., 1977. Understanding image intensities. *Artif. Intell.* 8, 201–231.
- Horn, B.K.P., 1981. Hill shading and the reflectance map. *Proc. IEEE* 69 (1), 14–47.
- Horn, B.K.P., Bachman, B.L., 1978. Using synthetic images to register real images with surface models. *Graph. Image Process.* 914–924.
- Kneissl, T., van Gassel, S., Neukum, G., 2011. Map-projection-independent crater size-frequency determination in GIS environments – new software tool for ArcGIS. *Planet. Space Sci.* 59, 1243–1254.
- Liu, B., Jia, M., Di, K., Oberst, J., Xu, B., Wan, W., 2017. Geopositioning precision analysis of multiple image triangulation using LROC NAC lunar images. *Planet. Space Sci.* <http://dx.doi.org/10.1016/j.pss.2017.07.016>.
- Liu, B., Xu, B., Di, K., Jia, M., 2016. A solution to low fitting precision of planetary orbiter images caused by exposure time changing. In: *Proceedings of 23rd ISPRS Congress, Commission IV*, 12–19 July, Prague, Czech Republic, pp. 441–448.

- Liu, B., Liu, Y.L., Di, K.C., Sun, X.L., 2014. Block adjustment of Chang'E-1 images based on rational function model. In: Remote Sensing of the Environment: 18th National Symposium on Remote Sensing of China, International Society for Optics and Photonics. 9158, 91580G.
- Liu, Y., Di, K., 2011. Evaluation of rational function model for geometric modeling of Chang'E-1 CCD images. *International Achievements of the Photogrammetry, Remote Sensing and Spatial Information Sciences*, Vol. 38, Part 4/W25, ISPRS Workshop on Geospatial Data Infrastructure: from data acquisition and updating to smarter services, Guilin, China, October 20–21.
- Michael, G.G., 2003. Coordinate registration by automated crater recognition. *Planet. Space Sci.* 51, 563–568.
- Morel, J., Yu, G., 2009. ASIFT: a new framework for fully affine invariant image comparison. *SIAM J. Imag. Sci.* 2 (2), 438–469.
- Mitas, L., Mitasova, H., 1988. General variational approach to the interpolation problem. *Comput. Math. Appl.* 16 (12), 983–992.
- NAIF, 2014. Lunar Reconnaissance Orbiter Camera (LROC) instrument kernel v18. < [http://naif.jpl.nasa.gov/pub/naif/pds/data/lro-l-spice-6-v1.0/lrosp\\_1000](http://naif.jpl.nasa.gov/pub/naif/pds/data/lro-l-spice-6-v1.0/lrosp_1000) > .
- Nefian, A.V., Coltin, B., Fong, T., 2014. Apollo metric imagery registration to Lunar Orbiter Laser Altimetry. *Lunar Planet. Sci. Conf.* 45, 1679.
- Robinson, M.S., Brylow, S.M., Tschimmel, M., Humm, D., Lawrence, S.J., Thomas, P.C., Denevi, B.W., Bowman-Cisneros, E., Zerr, J., Ravine, M.A., Caplinger, M.A., Ghaemi, F.T., Schaffner, J.A., Malin, M.C., Mahanti, P., Bartels, A., Anderson, J., Tran, T.N., Eliason, E.M., McEwen, A.S., Turtle, E., Jolliff, B.L., Hiesinger, H., 2010. Lunar Reconnaissance Orbiter Camera (LROC) instrument overview. *Space Sci. Rev.* 150, 81–124.
- Soderblom, L.A., Kirk, R.L., 2003. Meter-scale 3-D models of the Martian surface from combining MOC and MOLA data. *Lunar Planet. Sci. Conf.* 34, 1730.
- Soderblom, L.A., Kirk, R.L., Herkenhoff, K.E., 2002. Accurate fine-scale topography for the Martian south polar region from combining MOLA profiles and MOC NA Images. *Lunar Planet. Sci. Conf.* 33, 1254.
- Wu, B., Guo, J., Hu, H., Li, Z., Chen, Y., 2013. Co-registration of lunar topographic models derived from Chang'E-1, SELENE, and LRO laser altimeter data based on a novel surface matching method. *Earth Planet. Sci. Lett.* 364, 68–84.
- Wu, B., Hu, H., Guo, J., 2014. Integration of Chang'E-2 imagery and LRO laser altimeter data with a combined block adjustment for precision lunar topographic modeling. *Earth Planet. Sci. Lett.* 391, 1–15.
- Wu, B., Liu, W.C., Grumpe, A., Wöhler, C., 2017. Construction of pixel-level resolution DEMs from monocular images by shape and albedo from shading constrained with low-resolution DEM. *ISPRS J. Photogramm. Remote Sens.* <http://dx.doi.org/10.1016/j.isprsjsprs.2017.03.007>.
- Xinhuanet, 2017. < [http://news.xinhuanet.com/2017-06/07/c\\_1121102466.htm](http://news.xinhuanet.com/2017-06/07/c_1121102466.htm) > (accessed 19 May 2018).
- Yoon, J., Shan, J., 2005. Combined adjustment of MOC stereo imagery and MOLA altimetry data. *Photogramm. Eng. Remote Sens.* 71 (10), 1179–1186.